

Nanoscale

Accepted Manuscript



This is an *Accepted Manuscript*, which has been through the Royal Society of Chemistry peer review process and has been accepted for publication.

Accepted Manuscripts are published online shortly after acceptance, before technical editing, formatting and proof reading. Using this free service, authors can make their results available to the community, in citable form, before we publish the edited article. We will replace this *Accepted Manuscript* with the edited and formatted *Advance Article* as soon as it is available.

You can find more information about *Accepted Manuscripts* in the [Information for Authors](#).

Please note that technical editing may introduce minor changes to the text and/or graphics, which may alter content. The journal's standard [Terms & Conditions](#) and the [Ethical guidelines](#) still apply. In no event shall the Royal Society of Chemistry be held responsible for any errors or omissions in this *Accepted Manuscript* or any consequences arising from the use of any information it contains.

Cite this: DOI: 10.1039/c0xx00000x

www.rsc.org/xxxxxx

ARTICLE TYPE

Bio-inspired inner-motile photocatalyst film: a magnetically actuated artificial cilia photocatalyst

Dunpu Zhang, Wei Wang, Fengping Peng, Jiahui Kou, Yaru Ni, Chunhua Lu*, Zhongzi Xu*

Abstract: A new type of inner-motile photocatalyst film is explored to enhance photocatalytic

5 performance using magnetically actuated artificial cilia. The inner-motile photocatalyst film is capable of generating flow and mixing on the microscale because it produces a motion similar to that of natural cilia when it is subjected to a rotational magnetic field. Compared with traditional photocatalyst films, the inner-motile photocatalyst film exhibits the unique ability of microfluidic manipulation. It uses an impactful and self-contained design to accelerate interior mass transfer and desorption of degradation

10 species. Moreover, the special cilia-like structures increase the surface area and light absorption.

Consequently, the photocatalytic activity of the inner-motile photocatalyst film is dramatically improved

to approximately 3.0 times that of the traditional planar film. The inner-motile photocatalyst film also

exhibits high photocatalytic durability and can be reused several times with ease. Furthermore, this

feasible yet versatile platform can be extended to other photocatalyst systems, such as the TiO₂, P25, ZnO,

15 and Co₃O₄ systems, to improve their photocatalytic performance.

1. Introduction

Photocatalysis offers a promising tool to establish a sustainable society because of its relevance to energy and environment concerns, such as photocatalytic water splitting, solar energy conversion, CO₂ capture, and pollutant degradation.¹⁻⁸ The use of photocatalysts lies at the heart of this promising technology to achieve high efficiency in full-scale applications. Photocatalysts are typically used in suspension with powdered form. Although the suspension systems usually exhibit high photocatalytic performance, their main drawback is that separation and recycling of the photocatalyst from the slurry system are difficult. The processes are laborious in view of practical applications, which limit their sustainable and widespread utilization. The incorporation of magnetic particle with photocatalyst provides a way to address this issue. The magnetic photocatalyst can be easily separated and collected from slurry system with the aid of external magnetic field.⁹⁻¹¹ However, the photocatalytic activities and stability would be negatively affected by the hybrid structure because the magnetic particle may serve as the photogenerated electron-hole recombination center and be photocorroded under the irradiation.^{12, 13} An intermediate insulator (e.g., SiO₂) between the magnetic particle and photocatalyst can inhibit the recombination of the electron-hole pairs.^{13, 14} But, the structural complexity would be a challenge to design and synthesis for scale-up applications.

Alternately, solid materials are used to immobilize the photocatalyst (e.g., photocatalyst films).¹⁵ Compared with suspension systems, photocatalyst films better facilitate the separation process, thereby allowing the photocatalysts to be regenerated and reused in a sustainable manner.¹⁶ Motivated by these advantages, researchers have directed intensive attention to the development of high-performance photocatalyst films based on rational catalyst design.^{17, 18} However, the photocatalytic performance of such films is synergistically affected by the

50 primary reactions: light harvesting, mass transfer, catalytic reaction, and reactivation of active sites.¹⁹ Traditional planar photocatalyst films suffer from the intrinsic limitations of low surface area, weak mass transfer, and deactivation, which restrict their photocatalytic activities.²⁰ Then, hierarchical porous materials and nanotube/nanorod arrays have been developed to improve the photocatalytic performance because they exhibit high surface area.²¹⁻²⁴ However, these photocatalyst films are usually used in a stationary state due to their inflexible characteristics. Thus, the mass transfer in the reaction systems is passively dependent on either the reagent diffusion or external stirring. This dependence leads to very poor mass transfer properties on the micro- and nanometer scales.²⁵ Recently, the development of microreactor technology, e.g., optofluidic microreactor device, has drawn enormous interests from many researchers due to their promising applications in enhancing photocatalytic performance. Compared to macroscale reactors, the microreactor possesses obvious advantages, including short reactant diffusion distances, large surface-to-volume ratios, and good light penetration through the entire reactor depth with the reactor dimension scaling down.²⁶⁻²⁸ Many photocatalytic microreactors with immobilized photocatalyst have already been developed and been proven to be a highly effective tool for photocatalytic activity enhancement.²⁹⁻³³ However, the conventional stirring technologies limit the scope of their applications in the miniaturized microreactor devices on these small scales, resulting in a major problem of mass transfer limitation in the platform.^{33, 34} New methods dedicated to fluid mixing on the micrometer scale include micropumps, syringe pumps and electromagnetic actuation, and fluid mixing driven by volume or mass flow can be achieved and controlled by these external mechanical pumps.^{35, 36} Unfortunately, the flow type generated by these passive mixing technologies in microreactors is typically laminar and the mass transport is none the less mainly

relied on diffusion.³⁷ A lack of efficient mass transfer will not only result in a lower reaction rate, but will also result in covering of the active sites by degradation species. These species damage and reduce the durability of the photocatalyst film. Therefore, the exploration of active photocatalyst films that accelerate mass transfer, especially at the microscale, and exhibit improved surface area, light harvesting ability and durability, is of importance and interest in reality.

Microorganisms manipulate fluids on the microscale using hair-like cilia on their surfaces.³⁸ These hair-like cilia serve as microfluidic actuators in the natural fluid manipulation mechanism. Moreover, a variety of artificial cilia systems have been developed to generate flow and mixing.³⁹⁻⁴³ Therefore, if ciliary structures are introduced to photocatalyst films, they have the potential to actively regulate the mass transfer by taking advantage of special inner-motile characteristics.

Here, we combine photocatalyst systems with the ciliary motion characteristic of magnetically actuated artificial cilia to form inner-motile photocatalyst films. These films can be actuated by rotational magnetic fields to mimic ciliary motions and move fluid on the microscale, thereby providing an important and self-contained methodology for accelerating interior mass transfer and the desorption of degradation species without being dependent on other mixing technologies. Moreover, the surface area and light absorption benefit from the special ciliary structures. Therefore, both the activity and durability of the photocatalyst film can be dramatically improved by this strategy. This system can act as a versatile platform for the design of other high-efficiency inner-motile photocatalyst films that are stable, easy to use, and reusable.

2. Experimental section

2.1 Materials

Poly(dimethylsiloxane) prepolymer and curing agent (PDMS, Sylgard 184) were obtained from Dow Corning (MI, USA), which were mixed in a 10:1 ratio. Cobalt powder was prepared by chemical vapor deposition method, purchased from Miyou Co., Ltd. Carboxyl graphene (G-COOH, 5 mg/mL) was obtained from XFNano Material Tech Co., Ltd with carboxyl ratio of 5.0 wt.%. Xylene and ethanol was of reactant quality. Titanium tetrafluoride (TiF₄) and titanium tetraisopropoxide (TTIP, 97%) was purchased from Sigma-Aldrich. The commercial P25 was obtained from Degussa Co., Ltd.

2.2 Preparation

Preparation of artificial cilia

The artificial cilia was prepared by magnetic-field-induced self-assembly of magnetic particles method. Typically, Cobalt powder (0.15 g, 1.5 wt.%), PDMS prepolymer (3.00 g, 30 wt.%), curing agent (0.30 g) and xylene (6.55 g) were mixed by vigorously mechanical stirring for 60 min to obtain the magnetic suspension. Then, the suspension was poured into a mold (20 × 20 × 1 mm³) and transformed to a homogeneous perpendicular magnetic field (900 mT) which was generated by a pair of electric coils. After the solvent evaporation and PDMS curing under 80 °C for 3 h, the self-supporting artificial cilia (A15) was obtained. The typical artificial cilia can be well repeated by the mentioned method.

Preparation of G-COOH coated ciliary array (ciliary array@G-COOH, AG)

Glow-discharge plasma (200 W, 5 min) treatment was adopted to modify the artificial cilia with hydrophilic functionalities. Then, the treated artificial cilia was immersed into a G-COOH solution (0.5 mg/mL) which was diluted with ethanol. When taken out and expelled residual G-COOH solution, the artificial cilia was dried under 500 mT magnetic field at 60 °C. The coating process was repeated three times to give a homogeneous G-COOH layer on the array.

Growth of catalyst (TiO₂) on AG (ciliary array@rG-COOH@TiO₂, AGT)

The growth of TiO₂ was based on hydrolysis and condensation of TiF₄. TiF₄ (0.03 mmol) was homogeneously dissolved in deionized water (50 mL). The obtained AG was placed into the above TiF₄ solution and maintained at 90 °C for 12 h in a Teflon-lined stainless steel autoclave. The final AGT was obtained after UV irradiation (14 W, λ=365 nm) in ethanol for 2 h to reduce the G-COOH.

P25 immobilized on AG (ciliary array@rG-COOH@P25, AGP)

The P25 coating on AG was obtained by a simple spin-coating technique. P25 (2.5 mmol) and TTIP (0.1 mmol) were mixed in ethanol (10 mL) and dispersed by ultrasonic for 30 min. The AG was fully covered by the P25-TTIP solution, then was spin-coated at 600 r/min for 10 s and quickly accelerated to 3000 r/min for 20 s. The P25 coating was obtained by two cycles spin-coating and dried at 100 °C for 12 h. A planar P25 film was also prepared by the same method.

2.3 Characterization

The morphologies were characterized by field emission scanning electron microscopy (FESEM, HITACHI, SU-8010, Japan) and stereoscopic microscopy (Nikon, ZSM 745T, Japan). Raman spectra were measured on a Labram HR800 spectrometer with 514 nm laser as the excitation source. Thin-film XRD measurements were performed using SmartLab (Rigaku) thin-film diffractometer with Cu Kα radiation (λ = 1.54 Å) and incident angle 1.0°. Diffuse reflectance spectra were collected on the 3101 UV-vis-NIR spectrophotometer.

2.4 Photocatalytic test

The Rhodamine B (RhB) was chosen as a model to test the photocatalytic performance of AGT under UV irradiation (14 W, λ=365 nm). The AGT (20 × 20 mm²) was vertically placed in a Petri disk containing 5 mL RhB aqueous (0.01 g/L, *i.e.*, 0.02 mM), following by external stirring (1500 rpm, *i.e.*, 25 Hz) for 1 h in the dark to establish the adsorption-desorption equilibrium. The photodegradation was initiated after exposed to UV irradiation, which was positioned 5 cm away from the AGT with average light intensity of 3.1 mW cm⁻². At the given time interval, the absorbance of the solution was measured with a 3101 UV-vis-NIR spectrophotometer by monitoring the variation of maximum absorption at 554.0 nm.

To demonstrate the significant role of the ciliary motion in the improvement of photocatalytic performance, a similar procedure was constructed with actuated AGT by rotation magnetic field. The rotational magnetic field was provided by a pair of flat circular permanent magnets (Neodymium, N52, ϕ 25 × 5 mm), which were symmetrically placed on a variable

frequency motor with distance of 30 mm. Finally, the stimulus was placed 10 mm below the sample with their surface parallel to the substrate and perpendicular to the array direction. The actuated frequencies were varied from 0 to 17.5 Hz with 3.5 Hz interval.

The photocatalytic performance of AGP was tested under the same condition as AGT described above.

3. Results and discussion

3.1 Fabrication of the inner-motile photocatalyst film

A schematic representation of the fabrication strategy is shown in Fig. S1. The artificial cilia with ciliary arrays on the surface is a flexible composite of magnetic particle (cobalt) and poly(dimethylsiloxane) (PDMS), and is fabricated by magnetic-field-induced self-assembly method (Fig. S1a, b and c). Then, the artificial cilia is treated by a glow-discharge plasma (Fig. S1d), and coated with a thin carboxyl graphene (G-COOH) film (Fig. S1e). Finally, TiO₂ is grown on the array surface, following by UV irradiation to reduce the G-COOH (rG-COOH, Fig. S1f). TiO₂ is chosen because it is one kind of well-known functional

environmental pollutant degradation.⁴⁴⁻⁴⁶ Under suitable light irradiation, electron-hole pairs can be generated by TiO₂, which are responsible for its photocatalytic ability. To achieve a high photocatalytic performance, the electron-hole pairs should be separated effectively before their recombination.⁴⁷ Therefore, nanocomposites of functionalized graphene and TiO₂ have shown obvious enhancement of photocatalytic performance.⁴⁸ The functionalized graphene can be chemically integrated with TiO₂ to provide more effective separation of electron-hole pairs because of the excellent mobility of charge carriers of graphene.²¹ On the other hand, the poor conductivity of the artificial cilia matrix may show harmful effect on the photocatalytic activity. Hence, the ciliary array surface is modified by G-COOH (ciliary array@G-COOH, AG), to form a conducting layer. Moreover, the presence of functional groups (-COOH) in G-COOH makes it an excellent supporter to anchor the photocatalyst.⁴⁹ TiO₂ is grown on the AG by liquid-phase deposition, following by UV irradiation to form the ciliary array@rG-COOH@TiO₂ inner-motile photocatalyst film (AGT).⁵⁰ Based on these results, more types of photocatalysts, such as P25, ZnO nanorods, and Co₃O₄ nanosheets, are deposited on the artificial cilia to investigate the versatility and generality of the inner-motile photocatalyst film.

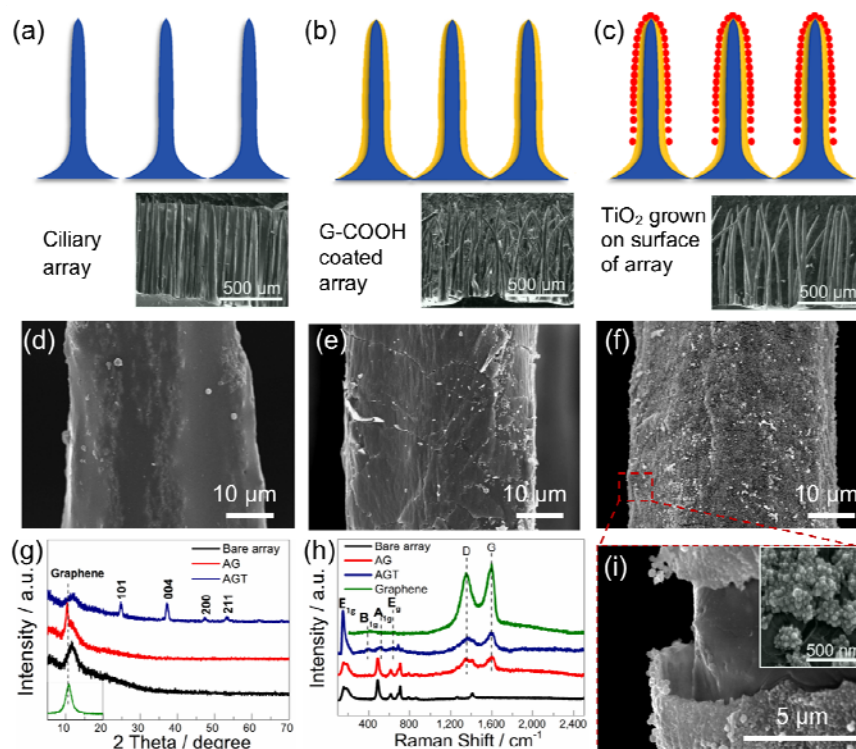


Fig. 1 Structural design of the AGT. Schematic and corresponding FESEM image of bare artificial cilia (a), AG (b), and AGT (c). Close-up FESEM images of the surface for bare artificial cilia (d), AG (e), and AGT (f). Phase characterization for the film-XRD patterns with an incident angle of 1.0° (g) and the Raman spectra (h). (i) Close-up FESEM image of the crack part of the AGT surface. The inset shows a high-magnification FESEM image of the AGT surface.

The fabrication of artificial cilia is based on previous work of our and Timonen's group.^{51, 52} First, cobalt particles were suspended in diluted PDMS prepolymer with solvent of xylene (Fig. S1a). Once a perpendicular magnetic field was applied, the magnetic particles assembled into linear chain structures, aligning along the direction of the magnetic field (Fig. S1b). Hence, the suspension was separated to a liquid phase and a solid particle chain phase.^{53, 54} As the liquid phase subsided with the

evaporation of solvent, the solid particle chain phase emerged above the liquid surface. The solid particle chains were encapsulated and stabilized by the PDMS polymer, resulting in the formation of conical-shaped ciliary array structure. Further, the residual PDMS in the suspension was left at the bottom as a flat film to support the conical-shaped ciliary arrays (Fig. S1c). After the PDMS cured, the self-supporting artificial cilia was obtained and could be easily peeled off from the mold. Fig. 1a

and S2 display the FESEM image and optical microscopy images of the typical artificial cilia, which was obtained with cobalt powder (1.5 wt.%) and PDMS prepolymer (30 wt.%) for 1 mm height of mold (A15). The artificial cilia is composed of uniform and well-aligned conical-shaped ciliary arrays on the surface with homogeneous spatial distribution. The ciliary array is approximately 920 μm in height and 40 μm in diameter, with a spacing of 220 μm . A plasma treatment was adopted to modify the hydrophobic array surface with hydrophilic functionalities (Fig. S1d), which ensured tight contact between the G-COOH film and the array.⁵⁵ The artificial cilia was immersed into a G-COOH solution and then removed and allowed to dry three times (Fig. S1e). After the treatment, a uniform G-COOH film is present on the ciliary array surface, as shown in the enlarged FESEM image (Fig. 1e). Fig. 1c illustrates the final morphology of the AGT. The surface-specific FESEM image (Fig. 1f) shows a rough surface on the array covered by dense TiO₂ nanoclusters. Moreover, a close-up image of the cracked part of the material (Fig. 1i) shows that the TiO₂ nanoclusters with diameters of ~300 nm are intimately bonded to the rG-COOH film.⁵⁶ Fig. 1g shows the thin-film XRD patterns of the composite structures. The diffraction peaks in the XRD pattern of the AGT can be assigned to anatase TiO₂ (JCPDS no. 01-089-4921).⁵⁷ Otherwise, no apparent peaks for graphene are observed in the pattern of AGT. However, the existence of graphene can be clearly elucidated by Raman analysis (Fig. 1h). Four characteristic scattering bands originating from the E_{g(1)}, B_{1g(1)}, A_{1g} + B_{1g(2)}, and E_{g(2)} modes of anatase TiO₂ are observed at 149, 399, 517 and 657 cm⁻¹, respectively, and the D and G bands of graphene at 1350 and 1595 cm⁻¹, respectively, are also shown. These results indicate the presence of anatase TiO₂ and graphene on the AGT.

The composite structure of TiO₂ deposited on rG-COOH film was further examined using TEM in Fig. S3. Fig. S3a,b reveals that the TiO₂ nanoclusters are well packed on the graphene in despite of intense ultrasonication treatment required for sample preparation, indicating the firm connection of TiO₂ and rG-COOH film. The high-resolution TEM image (HRTEM, Fig. S3c) shows clear parallel lattice fringes with spacing of 0.351 nm, corresponding to the (101) plane of anatase TiO₂. The diffraction rings of the selected area electron diffraction pattern (SAED, Fig. S3d) recorded for the nanoclusters suggest the polycrystalline nature of the anatase TiO₂.⁵⁸ The stable composite structure should be attributed to the formation of chemical bonding between TiO₂ and rG-COOH film. The reactive -COOH groups introduced by the G-COOH are able to chemically react with Ti cations in the solution, allowing the C-O-Ti bond to be formed for the initial heterogeneous nucleation.⁵⁹ This bond formation was explored by FTIR spectroscopy (Fig. S4). The new peak located at 800 cm⁻¹ can be assigned to the C-O-Ti vibration, which indicates firm TiO₂/rG-COOH chemisorption interfacial contact.^{60, 61}

The magnetic-field-induced self-assembly method is template-free and does not require special equipment. It allows the preparation of artificial cilia with various heights, densities, and dimensions. The array height can be easily varied by changing the height of the mold (e.g., 1, 2 and 3 mm). As shown in Fig. S5, the array density (the average number of cilia for 1 cm²) is approximately 890, 1140, and 2310 cilia/cm² for

magnetic particle concentration of 0.9 wt.% (A/AGT09), 1.2 wt.% (A/AGT12), and 1.5 wt.% (A/AGT15), respectively. Although the typical dimensions employed here are 20 \times 20 mm², uniform artificial cilia with dimensions as large as 50 \times 50 mm² can be successfully prepared. A macroscopic view of the sample is shown in Fig. S6. This flexibility in structural control is a distinct advantage for facilitating optimization and scale-up applications.

3.2 Magnetically actuated performance of AGT

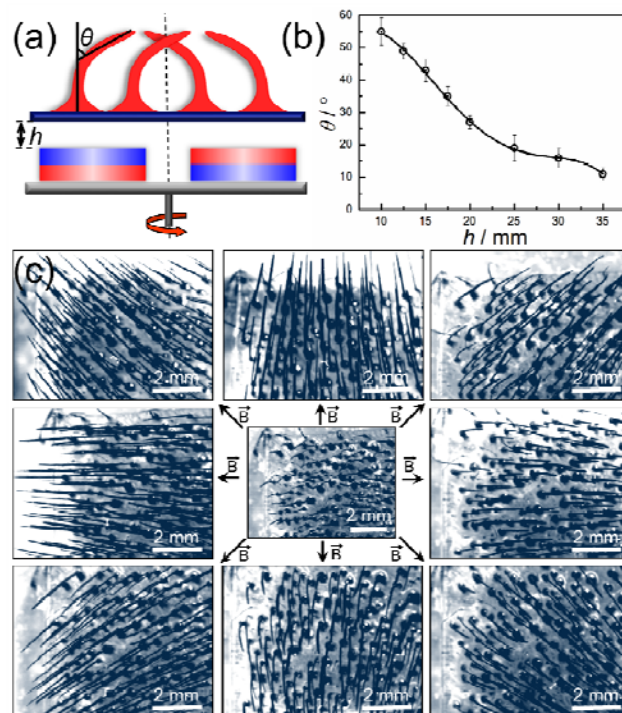


Fig. 2 The magnetically actuated AGT. (a) Schematic of the actuated AGT. (b) The tilt angle θ and the distance h for the AGT and the actuated magnet. (c) Optical micrograph sequences of the magnetic-field-induced bending of the AGT along the rotational directions of the magnetic field lines

The artificial cilia possesses two sophisticated characteristics in air and liquid: high mechanical stability and structural flexibility. Hence, the artificial cilia is self-supporting, yet can be bended to any specific angle and shape (Fig. S7 and S8). Significantly, these characteristics are inherited by the integrated AGT. When subjected to a magnetic field, the AGT rapidly responds to the applied field by bending to align along the local magnetic field lines.³⁸ To actuate the AGT, a pair of flat permanent magnets (neodymium, N52, Φ 25 mm) is rotated by a variable frequency motor as the stimulus. The tilt angle θ of the array with respect to the normal vector of the bottom is determined by the relative position h between the AGT and actuated magnet (Fig. 2a). The displacement of the 3 mm AGT15 under the actuated system is shown in Fig. 2b and S9. The tilt angle θ increases from 11.0 to 55.0° as the distance h decreases from 35 to 10 mm. The actuation movements under a rotational magnetic field are shown in Fig. 2c. These results indicate that the flexibility of our AGT structure imparts good actuation performance. The structures can be easily actuated with simple actuation equipment. The distance h was fixed at 10 mm for the

following actuation tests.

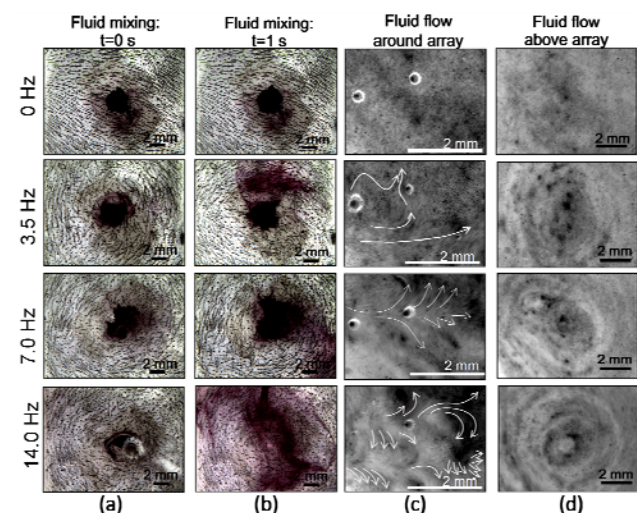


Fig. 3 Visualization of the fluidic mixing performance and the corresponding net fluid flow in an aqueous solution for the AGT under various actuation frequencies (0, 3.5, 7.0, and 14.0 Hz). Time-lapse flow mixing behaviors at the initial stage (a) and after 1 s (b). (c) Fluidic vortex distribution around the individual cilia. (d) Collective net flow fluctuation above the AGT.

When driven to mimic ciliary motion, the AGT can generate flow and mixing in solution. The mixing performance is well regulated via adjustment of the beat frequency. Fig. 3a,b show the mixing performance of the AGT in an aqueous solution under varied actuation frequencies compared with diffusive mixing. The boundary of injected dye aqueous is hardly expanded within 1.0 s for diffusive mixing process (0.0 Hz). In contrast, the dye aqueous shows a fast expansion and quick dispersion with the

aid of actuated AGT, and the mixing performance is enhanced with increasing the actuated frequency. The dye is disappeared within 10.0 s when being actuated at 3.5 Hz, and an almost homogeneous red aqueous is obtained within 1.0 s at 14.0 Hz. However, the dye aqueous can still be clearly seen in the case of diffusive mixing process within 10.0 s (Fig. S10). Clearly, the actuated AGT can accelerate the mass transfer, and thereby conduce to the homogenization of reactants. The mixing capability can be controlled through simply adjusting the actuation frequency. To further understand the effect of the flow, a particle tracking experiment was performed with video tracking of nonmagnetic hollow glass beads, which were used as passive trackers in the aqueous solution. This method can reveal the vortex distributions generated by each cilium and their contributions to collective flow fluctuation and mass transfer of the entire system. In Fig. 3c, an induced net vortex can be observed around the cilium of the AGT. This vortex is generated by the circulating motion of the artificial cilia. Comparison of the vortex patterns and distributions indicates that the induced flow vortices are greater when actuated at higher frequencies (Fig. S11). Above the tips of the AGT (Fig. 3d), collective net flow fluctuation is caused by thousands of ciliary arrays across the 10 mm diameter. At the microscale, these vortices vary randomly with time and space in terms of flow velocity and direction, which lead to irregular fluid motions that quickly disperse and homogenize the reactants.⁶² The enhancement in mass transfer by this inner-motile system provides an active mixing strategy that is conducive to photocatalytic performance.

3.3 Light absorption performance of the AGT

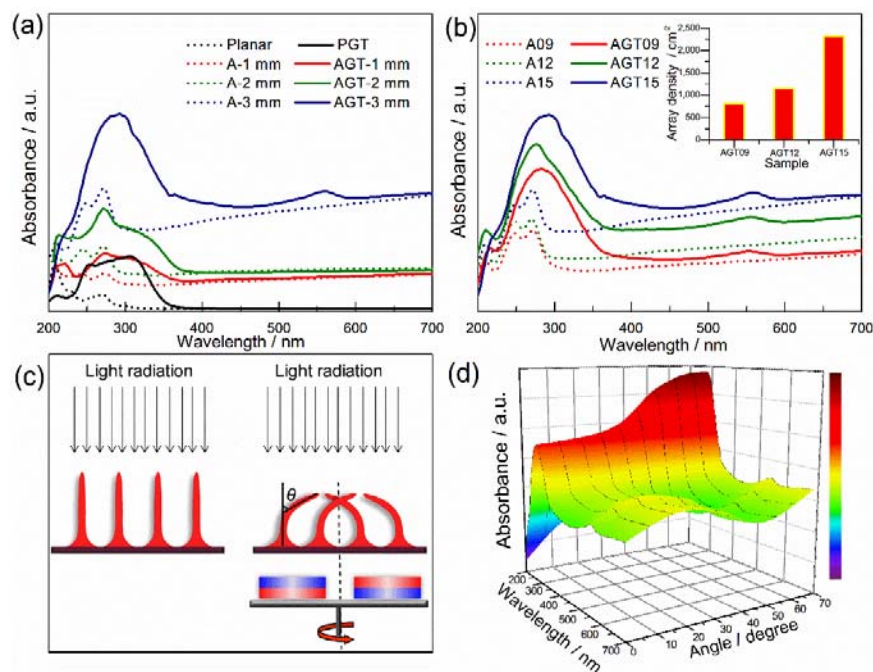


Fig. 4 Ultraviolet-visible absorption spectra for the AGT. (a) Absorption spectra for the AGT15 for various array heights (1, 2, and 3 mm) compared with the corresponding bare array. (b) Absorption spectra of the AGT for various array densities for 3 mm in height. Inset shows the corresponding array density. (c) Schematic of the angular dependent absorption of the bent AGT induced by the paired magnet. (d) The angular dependent absorption spectra for the 3 mm AGT15.

Cite this: DOI: 10.1039/c0xx00000x

www.rsc.org/xxxxxx

ARTICLE TYPE

The special structure of the AGT provides a promising solution to easily enhance surface area and light absorption through adjusting the structural parameters, such as the array height and density. Because of the large amount of ciliary arrays on the surface (up to 2310 cm^{-2} for the 3 mm AGT15), the array surface is nearly 10 times larger than that of the planar film. Moreover, the array can scatter the incident light in all directions because of the rough surface, resulting in long optical paths for efficient light usage. To reveal the effect of the array geometry and catalyst coating, we measured the absorption spectra of the AGT with different array heights and densities by ultraviolet-visible spectroscopy with an integrating sphere (transferred from reflectance, Fig. 4a,b).⁶³ For comparison, a planar PDMS film coated with G-COOH followed by TiO_2 (Planar@rG-COOH@ TiO_2 , PGT, Fig. S12) was measured. The array structure apparently improved the light-absorption performance compared with that of the planar structure. The increase in array height enhances light absorption. In the case of the AGT, an obvious change in the light absorption occurs from 270 to 400 nm, as shown in Fig. 4a, due to the intrinsic light response of the TiO_2 . Furthermore, a similar light-absorption trend is also observed for the AGT with different array densities (Fig. 4b). Thus, the AGT facilitates light absorption due to its special structure. The AGT light-absorption intensity is tunable via adjustment of the gemological parameters.

The optical measurements were all performed with incident light parallel to the array. However, when subjected to an actuated magnetic field, the array bends along the magnetic field (Fig. 4c), which would affect the light-absorption performance. Fig. 4d shows the angular dependence of the light absorption on the bent 3 mm AGT15. Clearly, the light absorption is enhanced with increased θ . This enhancement can be attributed to the greater optical contact area. Moreover, no obvious change in light absorption is observed as the AGT is actuated under various frequencies with fixed θ (Fig. S13), implying an independent absorption performance on actuated frequency.

3.4 Optimization of the AGT structure for improved photocatalytic performance

To assess the effect and optimization of the array structure on the photocatalytic activity, we measured the degradation of tetraethylated rhodamine B (RhB) by the AGT under UV irradiation (average light intensity: 3.1 mW cm^{-2}) with external stirring (25.0 Hz) (Fig. 5). The photocatalytic activities of three reference materials (PGT, bare array without TiO_2 , and the array without G-COOH modification (array/ TiO_2 , AT)) were also investigated. The bare array without TiO_2 exhibits very poor photocatalytic performance, similar to the self-degradation of RhB under UV irradiation. The photocatalytic performance dramatically improves when the TiO_2 is grown. The photocatalytic performance is improved by increasing array height (Fig. 5a). When the array height changes from 1 to 3 mm, the photocatalytic efficiency increases from 69% to 86%, which

is remarkably higher than that of PGT (52%). This increased efficiency can be attributed to the greater surface area and light absorption and is further confirmed by the fact that increased array density leads to increased photocatalytic performance (Fig. 5b). These results imply an innate advantage of the new photocatalyst film in terms of photocatalytic performance.

The performance of the AGT is enhanced when it is coated with rG-COOH because of the charge-transfer effect.⁶⁴ The TiO_2 nanoclusters are intimately bonded on rG-COOH film with direct chemical bonding (C-O-Ti). The high conductivity of rG-COOH implies high electron mobility, where the photogenerated electrons by TiO_2 can be quickly transferred through chemical bonding to prohibit the recombination of photogenerated electron-hole pairs.⁶⁰ The enhanced electron-hole pair separation increases the photocatalytic efficiency of the AGT (69%) compared with that of the AT (60%) over the same period.

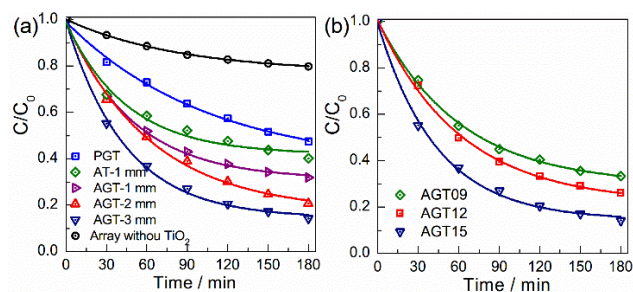


Fig. 5 Optimization of the AGT structure for enhanced photocatalytic performance. (a) Photocatalytic efficiency of the AGT15 of various heights (1, 2, and 3 mm) compared with a planar structure (PGT) and an array without rG-COOH (array/ TiO_2 , AT). (b) The photocatalytic efficiency of the 3 mm AGT with various array densities (AGT09/12/15). The frequency of external stirring was 25.0 Hz.

3.5 Photocatalytic performance of the AGT under magnetic actuation

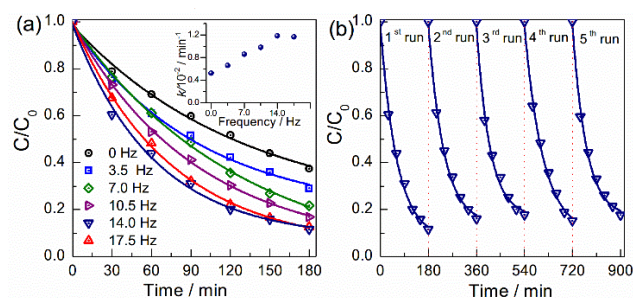


Fig. 6 Photocatalytic performance of the AGT under magnetic actuation. (a) Photocatalytic efficiencies under magnetic actuation at frequencies ranging from 0 to 17.5 Hz for the AGT15 with a height of 3 mm. The inset shows the apparent reaction rate constant k as a function of the actuation frequency. (b) The recycling stability of the AGT15 magnetically actuated at 14.0 Hz.

Our AGT are unique in their ability to perform active fluid mixing under driven by rotational magnetic fields. This is strikingly different from the stationary photocatalysts employed

in conventional photocatalytic methods. To demonstrate the significant role of the ciliary motion, the AGT was magnetically actuated for photocatalytic tests (Schematic drawing of experimental setup for the magnetically actuated photocatalytic test was shown in Fig. S14) with actuation frequencies ranging from 0 to 17.5 Hz for the 3 mm AGT15 (Fig. 6a). The actuated AGT exhibits higher photocatalytic efficiency compared with stationary film. The photocatalytic performance can be quantitatively evaluated by comparing the apparent reaction rate constants (k values, inset in Fig. 6a and S15).⁶⁴ A significant increase in the rate constant k is observed as the actuated frequency is gradually increased. The highest rate constant k is obtained at 14.0 Hz and corresponds to approximately 2.3 and 3.0 times that of the unactuated film (0 Hz) and the planar film, respectively. A slight decrease occurs when the frequency is further increased to 17.5 Hz. This may be attributed to that the ciliary array could not keep up the pace with the magnetic field under higher frequency (17.5 Hz), leading to the decrease of effective stroke, such as stroke frequency and stroke amplitude. Thus, the flow generated under 17.5 Hz is weakened as compared with that under 14.0 Hz, which shows effect on the mass transfer process in the reaction system. Therefore, more effective microfluidic generated at 14.0 Hz can conduct to more effective mass transfer process and higher photocatalytic performance. For comparison, the photocatalytic performance under external stirring with various frequencies was carried out (Fig. S16). The reaction rate k of the magnetically-actuated AGT is 1.4 times that of the externally stirred AGT at 14.0 Hz. Even if 25.0 Hz was used for externally stirred AGT, the reaction rate k is still lower than that of 14.0 Hz for magnetically actuated AGT. These results highlight the power and superiority of our proposed inner-motile photocatalyst film in enhancing the photocatalytic performance. Since the photocatalytic oxidant species, mainly hydroxyl and peroxy radicals, have very short lifetimes and are very easy to terminate, the photocatalytic reaction occurs mainly on the surface and/or in very close proximity of the photocatalyst.⁶⁵ To achieve high photocatalytic performance, pollutants should be effectively transported to the active sites to be degraded, following by continuous desorption of the degradation product to release the active sites. As illustrated in Fig. 7 and discussed previously, an intriguing advantage of this active system is that the motile AGT can serve as an efficient local microactuator to generate fluidic flow. The fluidic flow generated by the actuated AGT is able to strengthen the mass transfer and fast the motion of the RhB molecules to contact with the photocatalyst, meanwhile, the degradation products are easier to desorb from the surface of film, which are helpful to the enhancement of photocatalytic performance. Moreover, the new interior mass transfer strategy is an active and self-contained methodology without depending on other mixing technologies. To our knowledge, this combination of inner-motile characteristics and photocatalytic ability for dramatically improving the catalytic performance has not been reported previously.

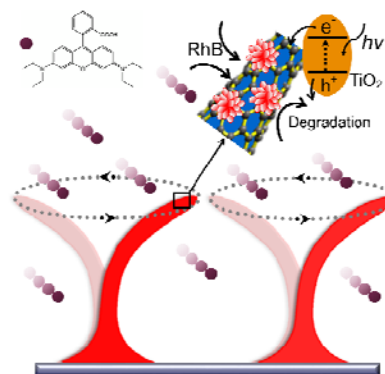


Fig. 7 Schematic structure and ciliary motion for interior mass transfer of the inner-motile photocatalyst film driven by a rotational magnetic field associated with the photocatalytic degradation of RhB.

The recycling stability of the magnetically actuated AGT was investigated in light of the practical applications for the 3 mm AGT15 at 14.0 Hz (Fig. 6b). The photocatalytic performance is maintained over several cycles without any significant changes. The performance can be maintained as high as 96% after five cycles. These results indicate that the AGT possesses a highly stable structure and can be easily reused several times. The high photocatalytic stability also highlights the reliability of the strategy for the development of other inner-motile materials.

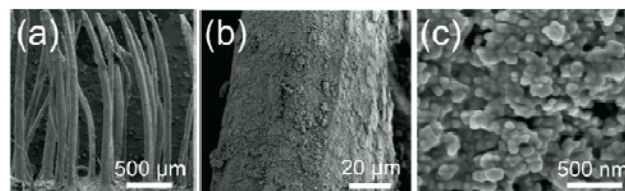


Fig. 8 FESEM images of the AGP at different magnifications

For a general-class catalyst film, the versatility in controlling the fundamental properties would determine the performance in various applications, specifically the ability to alter the catalyst type, morphology, and surface structure. The properties of our film can result in great improvements in the function of practical catalyst films. If the TiO₂ deposited on the AGT is replaced with other more active photocatalysts, such as P25, modified TiO₂, or TiO₂ nanosheets with exposed {001} facets, the inner-motile film may exhibit even more impressive photocatalytic performance. As a proof of concept, commercial Degussa P25 TiO₂ nanoparticles were deposited onto the AG with the aid of titanium tetraisopropoxide (TTIP), which can hydrolyze and bond the TiO₂ nanoparticles to form a uniform and stable layer (ciliary array@rG-COOH@P25, AGP).⁶⁶ The FESEM images of the AGP in Fig. 8 show that the interconnected P25 nanoparticles are closely packed on the surface of the array. Notably, the AGP actuated at 14.0 Hz exhibits a fast degradation rate, with 93% of the initial dye decomposed in 90 min (Fig. 9). The rate constant k is approximately 1.9 times that of a planar P25 film (Fig. S17). The photocatalytic performance of the AGP can be substantially improved by increasing the actuation frequency similar to that of AGT. This increase in actuation frequency also improves the performance compared with that of the stationary photocatalyst under external stirring. The optimal film thickness, film stability, and total catalyst loading will be

extensively studied in the future. However, the enhanced photocatalytic performance of the actuated AGP described here further demonstrates that the artificial cilia is an efficient and general platform for the development of high-performance photocatalyst films. The flexibility and generality of this technique can also be extended to other catalytic system with varied morphologies, such as ZnO nanorods and Co₃O₄ nanosheets grown on the array surface (Fig. S18). Moreover, the ability to tailor the catalyst properties allows the design of other types of catalyst films to target various functional applications (e.g., visible-light-driven photocatalyst films) and corresponding microreactor devices. These studies are in progress and will be reported in the near future.

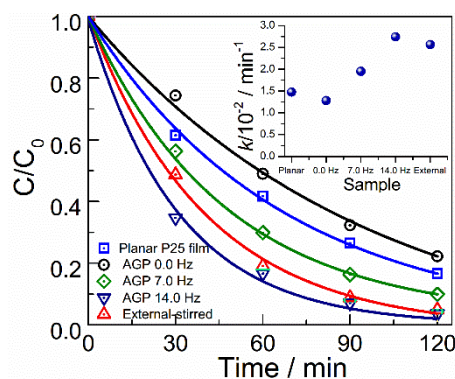


Fig. 9 Photocatalytic performance of the actuated AGP. The inset shows the apparent reaction rate constant k for the corresponding samples.

4. Conclusion

The new inner-motile photocatalyst film (AGT) based on magnetically actuated artificial cilia offers a promising active system for photocatalysis because of its efficient mixing capability, as well as enhanced surface area and light absorption. The photocatalytic performance of the AGT can be adjusted by controlling the physical geometry of the film (e.g., the array height and density). Flows generated by the actuated AGT promote efficient microfluidic mixing to overcome mass transfer limitation and facilitate desorption of degradation species. Compared with conventional stationary photocatalyst films, the AGT is better for photocatalysis because of its high performance and durability. This fundamental study shows that magnetically actuated artificial cilia are very useful for enhancing photocatalytic efficiency and providing new pathways to the design of high-activity photocatalyst films. Furthermore, the design of the inner-motile photocatalyst film can be extended to other catalyst systems, such as P25, ZnO, and Co₃O₄ systems, to improve their photocatalytic performance. The flexibility and generality of the platform will be applicable to more types of photocatalyst films with special functions designed for pollutant degradation, gas sensing, water splitting, and CO₂ photoreduction. As a consequence, it should strongly impact a wide range of catalytic processes. Moreover, our study demonstrates a general strategy to impart functionality to artificial cilia, and may open opportunities for designing various miniaturized devices for wide applications, such as biological diagnosis, drug delivery and chemical synthesis.

Acknowledgments

The authors were very thankful for the support from the Innovation Foundation for Graduate Students of Jiangsu Province China (CXLX11_0356), the National Natural Science Foundation of China (No. 51303079), and the Project Funded by the Priority Academic Program Development of Jiangsu Higher Education Institutions (PAPD).

Notes and references

State Key Laboratory of Materials-Orient Chemical Engineering, College of Materials Science and Engineering, Nanjing University of Technology, Nanjing 210009, People's Republic of China. Fax: +86 25 83587220, Tel.: +86 25 83587252, E-mail: chhlu@njtech.edu.cn; zzzxu@njtech.edu.cn.

† Electronic Supplementary Information (ESI) available: Additional data including details of fabrication scheme, TEM images of TiO₂ deposited on the G-COOH, optical microscopes of the artificial cilia, mechanical properties of the artificial cilia, details of mixing performance of actuated cilia, schematic drawing of experimental setup for photocatalytic test, photocatalytic kinetics curves, and the efficiency and generality of the new inner-motile photocatalyst film.. See DOI: 10.1039/b000000x/

References

- G. Xiong, R. Shao, T. C. Droubay, A. G. Joly, K. M. Beck, S. A. Chambers and W. P. Hess, *Adv. Funct. Mater.*, 2007, 17, 2133-2138.
- A. Y. Shan, T. I. M. Ghazi and S. A. Rashid, *Applied Catalysis A: General*, 2010, 389, 1-8.
- J. Ng, S. Xu, X. Zhang, H. Y. Yang and D. D. Sun, *Adv. Funct. Mater.*, 2010, 20, 4287-4294.
- D. V. Esposito, I. Levin, T. P. Moffat and A. A. Talin, *Nat. Mater.*, 2013, 12, 562-568.
- Z. Jiang, Y. Tang, Q. Tay, Y. Zhang, O. I. Malyi, D. Wang, J. Deng, Y. Lai, H. Zhou, X. Chen, Z. Dong and Z. Chen, *Adv. Energy Mater.*, 2013, 3, 1368-1380.
- N. Lu, Y. Zhao, H. Liu, Y. Guo, X. Yuan, H. Xu, H. Peng and H. Qin, *J Hazard. Mater.*, 2012, 199-200, 1-8.
- A. M. Balu, B. Baruwati, E. Serrano, J. Cot, J. Garcia-Martinez, R. S. Varma and R. Luque, *Green Chem.*, 2011, 13, 2750-2758.
- J. Wang, X. Yang, K. Zhao, P. Xu, L. Zong, R. Yu, D. Wang, J. Deng, J. Chen and X. Xing, *J. Mater. Chem., A*, 2013, 1, 9069-9074.
- S. Xuan, W. Jiang, X. Gong, Y. Hu and Z. Chen, *J. Phys. Chem. C*, 2008, 113, 553-558.
- Y. Liu, L. Yu, Y. Hu, C. Guo, F. Zhang and X. Wen Lou, *Nanoscale*, 2012, 4, 183-187.
- T. H. Yu, W. Y. Cheng, K. J. Chao and S. Y. Lu, *Nanoscale*, 2013, 5, 7356-7360.
- D. Beydoun, R. Amal, G. Low and S. McEvoy, *J. Mol. Catal. A: Chem.*, 2002, 180, 193-200.
- S. Q. Liu, *Environ. Chem. Lett.*, 2012, 10, 209-216.
- H. Wang, X. Fei, L. Wang, Y. Li, S. Xu, M. Sun, L. Sun, C. Zhang, Y. Li, Q. Yang and Y. Wei, *New J. Chem.*, 2011, 35, 1795-1802.
- S. I. In, A. H. Kean, A. Orlov, M. S. Tikhov and R. M. Lambert, *Energy Environ. Sci.*, 2009, 2, 1277-1279.
- J. Marugán, M. J. López-Muñoz, R. van Grieken and J. Aguado, *Ind. Eng. Chem. Res.*, 2007, 46, 7605-7610.
- R. Asahi, T. Morikawa, T. Ohwaki, K. Aoki and Y. Taga, *Science*, 2001, 293, 269-271.
- Q. Li, W. Liang and J. K. Shang, *Appl. Phys. Lett.*, 2007, 90, 063109.
- D. Buso, J. Pacifico, A. Martucci and P. Mulvaney, *Adv. Funct. Mater.*, 2007, 17, 347-354.
- R. Portela, S. Suárez, R. F. Tessinari, M. D. Hernández-Alonso, M. C. Canela and B. Sánchez, *Appl. Catal., B*, 2011, 105, 95-102.
- J. Du, X. Lai, N. Yang, J. Zhai, D. Kisailus, F. Su, D. Wang and L. Jiang, *ACS Nano*, 2010, 5, 590-596.
- G. R. Meseck, R. Kontic, G. R. Patzke and S. Seeger, *Adv. Funct. Mater.*, 2012, 22, 4433-4438.
- C. J. Lin, Y. H. Yu and Y. H. Liou, *Appl. Catal., B*, 2009, 93, 119-125.

24. S. Jung and K. Yong, *Chem. Commun.*, 2011, 47, 2643-2645.
25. A. Corma, *J. Catal.*, 2003, 216, 298-312.
26. R. Gorges, S. Meyer and G. Kreisel, *J. Photochem. Photobiol., A*, 2004, 167, 95-99.
27. M. Krivec, K. Žagar, L. Suhadolnik, M. Čeh and G. Dražič, *ACS Appl. Mater. Interfaces*, 2013, 5, 9088-9094.
28. H. Lu, M. A. Schmidt and K. F. Jensen, *Lab Chip*, 2001, 1, 22-28.
29. H. Lin and K. Valsaraj, *J. Appl. Electrochem.*, 2005, 35, 699-708.
30. S. Teekateerawej, J. Nishino and Y. Nosaka, *J. Appl. Electrochem.*, 2005, 35, 693-697.
31. K. Natarajan, T. S. Natarajan, H. C. Bajaj and R. J. Tayade, *Chem. Eng. J.*, 2011, 178, 40-49.
32. Z. Meng, X. Zhang and J. Qin, *Nanoscale*, 2013, 5, 4687-4690.
33. H. J. Koo and O. D. Velev, *J. Mater. Chem., A*, 2013, 1, 11106-11110.
34. S. Khaderi, J. Hussong, J. Westerweel, J. d. Toonder and P. Onck, *RSC Adv.*, 2013, 3, 12735.
35. S. N. Khaderi, J. M. J. den Toonder and P. R. Onck, *Langmuir*, 2012, 28, 7921-7937.
36. J. Hussong, N. Schorr, J. Belardi, O. Prucker, J. Ruhe and J. Westerweel, *Lab Chip*, 2011, 11, 2017-2022.
37. L. Li, R. Chen, X. Zhu, H. Wang, Y. Wang, Q. Liao and D. Wang, *ACS Appl. Mater. Interfaces*, 2013, 5, 12548-12553.
38. A. R. Shields, B. L. Fiser, B. A. Evans, M. R. Falvo, S. Washburn and R. Superfine, *Proc. Natl. Acad. Sci. U.S.A.*, 2010, 107, 15670-15675.
39. J. d. Toonder and P. R. Onck, *Trends Biotechnol.*, 2013, 31, 85-91.
40. J. d. Toonder, F. Bos, D. Broer, L. Filippini, M. Gillies, J. de Goede, T. Mol, M. Reijme, W. Talen, H. Wilderbeek, V. Khatavkar and P. Anderson, *Lab Chip*, 2008, 8, 533-541.
41. S. N. Khaderi, C. B. Craus, J. Hussong, N. Schorr, J. Belardi, J. Westerweel, O. Prucker, J. Ruhe, J. M. J. den Toonder and P. R. Onck, *Lab Chip*, 2011, 11, 2002-2010.
42. B. A. Evans, A. R. Shields, R. L. Carroll, S. Washburn, M. R. Falvo and R. Superfine, *Nano Lett.*, 2007, 7, 1428-1434.
43. C. L. van Oosten, C. W. M. Bastiaansen and D. J. Broer, *Nat. Mater.*, 2009, 8, 677-682.
44. J. B. Joo, I. Lee, M. Dahl, G. D. Moon, F. Zaera and Y. Yin, *Adv. Funct. Mater.*, 2013, 23, 4246-4254.
45. C. Liu, Z. Lei, Y. Yang and Z. Zhang, *Water Res.*, 2013, 47, 4986-4992.
46. X. Cao, Z. Lu, L. Zhu, L. Yang, L. Gu, L. Cai and J. Chen, *Nanoscale*, 2014, DOI: 10.1039/C3NR04785G.
47. M. S. A. Sher Shah, A. R. Park, K. Zhang, J. H. Park and P. J. Yoo, *ACS Appl. Mater. Interfaces*, 2012, 4, 3893-3901.
48. G. Williams, B. Seger and P. V. Kamat, *ACS Nano*, 2008, 2, 1487-1491.
49. N. J. Bell, Y. H. Ng, A. Du, H. Coster, S. C. Smith and R. Amal, *J. Phys. Chem. C*, 2011, 115, 6004-6009.
50. J. Liu, H. Bai, Y. Wang, Z. Liu, X. Zhang and D. D. Sun, *Adv. Funct. Mater.*, 2010, 20, 4175-4181.
51. D. Xu, C. H. Lu, D. P. Zhang, J. Song, Y. Ni and Z. Z. Xu, *Mater. Lett.*, 2012, 71, 94-97.
52. J. V. Timonen, C. Johans, K. Kontturi, A. Walther, O. Ikkala and R. H. Ras, *ACS Appl. Mater. Interfaces*, 2010, 2, 2226-2230.
53. M. Ivey, J. Liu, Y. Zhu and S. Cutillas, *Phys. Rev. E*, 2000, 63, 011403.
54. W. Fang, Z. He, X. Xu, Z. Mao and H. Shen, *Europhys. Lett.*, 2007, 77, 68004.
55. L. Cai, J. Li, P. Luan, H. Dong, D. Zhao, Q. Zhang, X. Zhang, M. Tu, Q. Zeng, W. Zhou and S. Xie, *Adv. Funct. Mater.*, 2012, 22, 5238-5244.
56. W. Tu, Y. Zhou, Q. Liu, S. Yan, S. Bao, X. Wang, M. Xiao and Z. Zou, *Adv. Funct. Mater.*, 2013, 23, 1743-1749.
57. Q. Huang, S. Tian, D. Zeng, X. Wang, W. Song, Y. Li, W. Xiao and C. Xie, *ACS Catalysis*, 2013, 1477-1485.
58. C. Chen, W. Cai, M. Long, B. Zhou, Y. Wu, D. Wu and Y. Feng, *ACS Nano*, 2010, 4, 6425-6432.
59. H. G. Yang and H. C. Zeng, *J. Phys. Chem. B*, 2003, 107, 12244-12255.
60. H. Zhang, X. Lv, Y. Li, Y. Wang and J. Li, *ACS Nano*, 2009, 4, 380-386.
61. S. Wang, L. Yi, J. E. Halpert, X. Lai, Y. Liu, H. Cao, R. Yu, D. Wang and Y. Li, *Small*, 2012, 8, 265-271.
62. N. Nam-Trung and W. Zhigang, *J. Micromech. Microeng.*, 2005, 15, R1.
63. X. Xu, C. Random, P. Efstathiou and J. T. S. Irvine, *Nat. Mater.*, 2012, 11, 595-598.
64. N. Yang, Y. Liu, H. Wen, Z. Tang, H. Zhao, Y. Li and D. Wang, *ACS Nano*, 2013, 7, 1504-1512.
65. A. Zhang, M. Zhou, L. Han and Q. Zhou, *J. Hazard. Mater.*, 2011, 186, 1374-1383.
66. D. Zhang, T. Yoshida, T. Oekermann, K. Furuta and H. Minoura, *Adv. Funct. Mater.*, 2006, 16, 1228-1234.